# Electroencephalography (EEG)-near-infrared spectroscopy (NIRS) based online imaging during non-invasive electrical brain stimulation

Anirban Dutta

**Master of Science in Cerebrovascular Medicine**

Master Thesis

# Electroencephalography (EEG)-near-infrared spectroscopy (NIRS) based online imaging during non-invasive electrical brain stimulation

By: Anirban Dutta, Ph.D.

Matriculation Number: 218694

Date of submission: 09/30/2014

Direct supervisor: Michael A. Nitsche, M.D.

| Name and address of responsible research group leader: | Name and address of suggested second reviewer: |
|---|---|
| Jens P. Dreier, M.D. | Jens Steinbrink, Ph.D. |

## Chapter 1 - Introduction

Transcranial direct current stimulation (tDCS) has been shown to modulate cortical neural activity (Nitsche and Paulus 2000). During neural activity, the electric currents from excitable membranes of brain tissue superimpose at a given location in the extracellular medium and generate a potential, which is referred to as the electroencephalogram (EEG) when recorded from the scalp (Nunez and Srinivasan 2006). Respective neural activity has been shown to be closely related, spatially and temporally, to cerebral blood flow (CBF) that supplies glucose via neurovascular coupling (Girouard and Iadecola 2006). The hemodynamic response to neural activity can be captured by near-infrared spectroscopy (NIRS), which enables continuous monitoring of cerebral oxygenation and blood volume (Siesler et al. 2008). Here, the CBF is increased in the brain regions with neural activity via metabolic coupling mechanisms (Attwell et al. 2010). Cerebral autoregulation mechanisms ensure that the blood flow is maintained during changes in the perfusion pressure (Lucas et al. 2010). We proposed a phenomological model for metabolic coupling mechanisms (Attwell et al. 2010) to capture cerebrovascular reactivity (CVR) that represented the capacity of blood vessels to dilate during anodal tDCS due to neuronal activity-caused increased demands of oxygen (Dutta et al. 2013). Cross-sectional studies suggest that impaired cerebral hemodynamics precedes stroke and transient ischaemic attacks (TIA). CVR reflects the capacity of blood vessels to dilate, and is an important marker for brain vascular reserve (Markus and Cullinane 2001). Therefore, cerebrovascular reserve capacity may have a predictive value for the risk of cerebral infarction in patients with reduced cerebrovascular reserve capacity such that it might evolve as a part of routine diagnostic neuroangiologic program (Stoll and Hamann 2002).

### *A. Phenomological model for capturing cerebrovascular reactivity to anodal tDCS*

The regulation of CBF and its distribution may be probed with anodal tDCS which challenges the system with a vasoactive stimulus in order to observe the system response. During such an experiment, CVR can be measured as the change in CBF per unit change in relation to anodal tDCS intensity. Prior work has shown a significant correlation between tDCS current strength and increase in regional CBF in the on-period relative to the pre-stimulation baseline (Zheng et al. 2011). In our preliminary study, we investigated regional CVR during anodal tDCS by adapting an arteriolar

compliance model of the cerebral blood flow response to a neural stimulus (Behzadi and Liu 2005). Regional CVR was defined as the coupling between changes in CBF and cerebral metabolic rate of oxygen (CMRO2) during anodal tDCS-induced local brain activation (Leontiev and Buxton 2007). The complex path from tDCS-induced change in synaptic transmembrane current, $u(t)$ (only excitatory considered) (Molaee-Ardekani et al. 2013) to a change in the concentration of multiple vasoactive agents (such as NO, potassium ions, adenosine) represented by a single vascular flow-inducing vasoactive signal, $s$, was captured by a first-order Friston's model (Friston et al. 2000).

$$\dot{s} = \varepsilon u(t) - k_s s - g_f(f-1) \quad (1)$$

where $f$ denoted CBF normalized by its baseline value, $\varepsilon$ is the neuronal efficacy, $k_s$ is the rate constant for signal decay, and $g_f$ is the gain constant for an auto-regulatory feedback term that drives the CBF back to its baseline value (at steady state: $\dot{s} = 0$, $s = 0$ and $u(t) = g_f(f-1)/\varepsilon$ i.e. synaptic transmembrane current correlated with baseline-normalized CBF at steady state). The released vasoactive signal, $s$, changes the compliance, $C$, of the vasculature approximated by first-order kinetics, leading to changes in its representative radius, $R$, that can be captured by a nonlinear compliance model (Behzadi and Liu 2005). For ease in NIRS data fitting, the nonlinear compliance model was linearized about an equilibrium point $C_M$, and the radius, $R$, was approximated as,

$$\dot{C} = s$$
$$R \approx R_{\max}(1 - a_1 \exp(-a_2 C_M)) \quad (2)$$

where $R_{\max}$ is the maximum radius, and $a_1$ and $a_2$ are constants. The CBF, i.e., the volume of blood that flows through a unit volume of tissue in a unit time can be approximated using Ohmic equation,

$$CBF = K(P_a - P_v)R^{\gamma}$$

where $P_a$ and $P_v$ are arterial and venous blood pressures respectively, K is a constant of proportionality, and the exponent $\gamma$ is 2 for plug-flow and 4 for laminar flow. Here, anodal tDCS is assumed to change CBF via synaptic transmembrane current, $u(t)$, leading to changes only in $R$ and

not in blood pressure difference $(P_a - P_v)$. However, bihemispheric effects of tDCS on cerebral vasomotor reactivity (Vernieri et al. 2010) supports an additional systemic effect which we will neglect to simplify the model. Under this simplifying assumption, the baseline-normalized CBF, $f$, can be approximated as,

$$f = \left( \frac{R}{R_0} \right)^{\gamma} \tag{3}$$

where $R_0$ is the radius of tissue vasculature at baseline. Since NIRS measures changes in tissue oxy-($HbO2$), and deoxy-($Hb$) hemoglobin concentration, these need to be approximated based on $f$. So a third hemodynamic variable, $Hbt$, was derived as the sum of $HbO2$ and $Hb$ concentrations, which is considered a good indicator of variations in the regional cerebral blood volume, $Vol_{blood}$ (Villringer and Chance 1997). Under the assumption that the tissue vasculature has a volume, $Vol_{vasc}$, proportional to $R^2$ and haematocrit remains constant, the changes in tissue total ($Hbt$) hemoglobin concentration can be approximated as (Boas et al. 2003),

$$\begin{aligned}
&\frac{Vol_{vasc}}{Vol_{vasc,0}} = \frac{R^2}{R_0^{\,2}} \\
&\Rightarrow \frac{Vol_{blood}}{Vol_{blood,0}} = \frac{R^2}{R_0^{\,2}} \\
&\Rightarrow \frac{Hbt}{Hbt_0} = \frac{R^2}{R_0^{\,2}}, \ \because \text{ haematocrit constant} \\
&\Rightarrow f = \left( \frac{Hbt}{Hbt_0} \right)^{\gamma/2}
\end{aligned} \tag{4}$$

The cerebral metabolic rate of oxygen, $CMRO2$ (i.e., oxygen consumption), is given by the difference of oxygen flowing into and out of the tissue (Boas et al. 2003). Assuming that the arterial oxygen concentration, $C_A$, is unaffected by anodal tDCS (Behzadi and Liu 2005), $CMRO2$ can be related to CBF as,

$$\begin{aligned}
&CMRO2 = E \cdot C_A \cdot CBF \\
&\Rightarrow \frac{CMRO2}{CMRO2_0} = \frac{E(f, E_0)}{E_0} f
\end{aligned}$$

where $E$ is the extraction fraction of oxygen ($E_0$ at baseline). The CVR was defined as the ratio between fractional CBF change and fractional CMRO2 change from baseline, $CVR = \frac{CMRO2 / CMRO2_0}{f} \Rightarrow CVR = \frac{E(f, E_0)}{E_0}$. The baseline-normalized CMRO2 (i.e. $CVR \cdot f$) can be estimated from baseline-normalized tissue CBF ($f$), and deoxy- ($Hb$) and total ($Hbt$) hemoglobin concentration using the ratio method (Boas et al. 2003),

$$\left(1+\frac{CMRO2}{CMRO2_0}\right) = (1+f)\left(1+\gamma_R \frac{Hb}{Hb_0}\right)\left(1+\gamma_T \frac{Hbt}{Hbt_0}\right)^{-1} \text{ from [19]}$$
$$\Rightarrow (1+CVR \cdot f) = (1+f)\left(1+\gamma_R \frac{Hb}{Hb_0}\right)\left(1+\gamma_T \frac{Hbt}{Hbt_0}\right)^{-1}$$
$$\Rightarrow \left(1+CVR \cdot \left(\frac{Hbt}{Hbt_0}\right)^{\gamma/2}\right) = \left(1+\left(\frac{Hbt}{Hbt_0}\right)^{\gamma/2}\right)\left(1+\gamma_R \frac{Hb}{Hb_0}\right)\left(1+\gamma_T \frac{Hbt}{Hbt_0}\right)^{-1} \quad (5)$$

where the factors $\gamma_R \in [0.5, 1.5];\ \gamma_T \in [0.5, 1.5]$ related fractional hemoglobin changes in the venous compartment to those across all vascular components, and $SO2_0$ relates oxygen saturation at baseline of the venous compartment to $Hbt_0$ (Boas et al. 2003), $SO2_0 = \frac{HbO2_0}{Hb_0 + HbO2_0} \Rightarrow SO2_0 = \frac{Hbt_0 - Hb_0}{Hbt_0}$.

In diffusion-limited oxygen delivery (Buxton and Frank 1997), oxygen consumption is limited by diffusion of oxygen from the vasculature and thus oxygen consumption is tightly coupled to induced blood flow (Boas et al. 2003) and the surface area of the vasculature (i.e. proportional to $R$). A neural mass model (Dutta and Nitsche 2013) relating anodal tDCS strength (current density), $\sigma(t)$, to tDCS-induced changes in synaptic transmembrane current, $u(t)$ (Molaee-Ardekani et al. 2013) can be coupled with the neurovascular model (i.e., equations 1-4) representing the hemodynamic ($Hbt$) response to anodal tDCS, $\sigma(t)$, where deoxy- ($Hb$) is a byproduct of the consumption of oxygen delivered by oxy- ($HbO2$) hemoglobin that can be estimated using the cerebral metabolic rate of oxygen, $CMRO2$ (and $CVR = \frac{E(f, E_0)}{E_0}$) (Dutta et al. 2013).

### *B. Neural mass model for capturing neuronal response to anodal tDCS*

Neural mass models (NMM) provide insights into the neuromodulatory mechanisms underlying alterations of cortical activity induced via tDCS (Molaee-Ardekani et al. 2013). In our prior work, we aimed to capture the origin of tDCS-induced alterations in the electroencephalography (EEG) power spectrum using a thalamocortical NMM (Dutta and Nitsche 2013), we found that anodal tDCS enhances activity and excitability of the excitatory pyramidal neuron at a population level in a non-specific manner, and that μ-rhythm desynchronization is generated. The NMM for a single cortical source comprised of 4 neuronal subpopulations, excitatory pyramidal neurons (ePN), excitatory interneurons (eIN), slow inhibitory interneurons (siIN), and fast inhibitory interneurons (fiIN) (Zavaglia et al. 2006). The NMM for the cortical source was coupled with another representing the thalamus (Sotero et al. 2007), which comprised of 2 neuronal subpopulations - an excitatory thalamocortical (eTCN) and an inhibitory reticular-thalamic (iRT). The basis of our cortical NMM is the Friston model (Moran et al. 2007) that emulates the activity of a cortical area using three neuronal subpopulations, ePN, eIN, and siIN. A population of ePN (output) cells receives inputs from inhibitory and excitatory populations of interneurons via intrinsic connections (intrinsic connections are confined to the cortical sheet). An extrinsic thalamo–cortico–thalamic loop consists of eTCN and iRT in the thalamic NMM (Ursino et al. 2010). The lumped thalamo–cortico–thalamic network model can be used to simulate the subject-specific EEG power spectral density changes during/following tDCS (Dutta and Nitsche 2013) by modifying the model parameters (e.g., average gain of synapses, their time constants) (Zavaglia et al. 2006). Specifically, each neuronal subpopulation has an average membrane potential, $V_i$ (i=ePN, eIN, siIN, eTCN, iRT), which serves as input for a sigmoid function that converts it into average density of spikes, $Z_i$ (i=ePN, eIN, siIN, eTCN, iRT), fired by the respective neuronal subpopulation (Moran et al. 2007). This output from neuronal subpopulations enters synapses (excitatory or inhibitory) via a second order linear function. The second order differential equation representing the synapses is described by a lumped gain, $G_i$, and a lumped time constant, $\tau_i$,

$$\ddot{Y}_i(t) = G_i \frac{1}{\tau_i} Z_i(t) - 2\frac{1}{\tau_i}\dot{Y}_i(t) - \left(\frac{1}{\tau_i}\right)_i^2 Y_i(t) \quad (6)$$

where $Y_i$ (i=ePN, eIN, siIN, eTCN, iRT) represents the postsynaptic membrane potentials, which can be excitatory or inhibitory. Interactions among neuronal subpopulations are modeled via connectivity constants, $C_{ij}$(i,j=ePN, eIN, siIN, eTCN, iRT), which scale the postsynaptic membrane potentials, $Y_i$, from various synaptic inputs to produce alterations of the lumped membrane potential, $V_i$, at the soma. Therefore, membrane potential alterations of ePN represent synaptic inputs from all interconnected neuronal subpopulations. The membrane potential alterations of ePN was used as an estimator of the EEG power spectral density in our case based on prior work (Zavaglia et al. 2006), however, transmembrane current is a more reliable estimator (Buzsáki et al. 2012). A Gaussian white noise input, $I(t)$, with a mean, $m(t)$, and variance, $\sigma^2$, was provided to the ePN subpopulation. Equation 6 transforms the average density of spikes, $Z_i$, arriving as presynaptic input into average postsynaptic membrane potentials, $Y_i$. This can be modeled by convolving $Z_i$ with synaptic impulse response function (sIRF) of the dendritic tree (Moran et al. 2007).

$$Y_i(t) = sIRF_i(t) \otimes Z_i(t)$$
$$sIRF_i(t) = G_i \frac{1}{\tau_i} t \exp\left(-\frac{t}{\tau_i}\right) \quad (7)$$

The parameter, $G_i$, tunes the maximum amplitude of the postsynaptic membrane potential and the parameter, $\tau_i$, is a lumped representation of the sum of the rate constants of the membrane and other spatially distributed delays in the dendritic tree.

The excitation versus inhibition effects of acute tDCS on the population kinetics can produce a whole spectrum of EEG signals within the oscillatory regime of a neural mass model (David and Friston 2003). The effects on the population kinetics depends on the direction of cortical current flow determining the relative influence of acute tDCS on the cellular targets responsible for the modulation of synaptic efficacy, which are primarily somata and axon terminals (Rahman et al. 2013). Therefore, not all neural tissue will be equally affected by a given stimulation protocol which may distinctly affect neuronal populations/neuronal compartments. Here, basal and apical dendrites can be concomitantly polarized in opposite directions, and Layer V pyramidal neurons exhibit the highest measured somatic sensitivities to subthreshold fields (Rahman et al. 2013). Therefore, somatic depolarization of Layer V

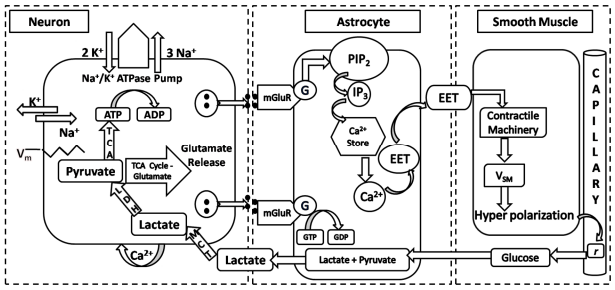


Figure 1.1: Schematic of biochemical signaling from neuron→astrocyte→vessel→neuron coupling, taken from (Chander and Chakravarthy 2012).

pyramidal neurons with anodal tDCS may result in corresponding alterations of spontaneous firing rate (Radman et al. 2009) thereby causing a rapid increase in extracellular potassium concentration due to outwardly directed potassium currents (Holthoff and Witte 2000). The glial network has an important role in regulating neural activity by distributing extracellular potassium, i.e. spatial buffering, which can have a time course of seconds (Halnes et al. 2013). Due to this relatively long time course, some of these diffusing extracellular potassium ions can act as mediators of vasodilation (Eckman and Nelson 2001) as well as neurotransmitters, affecting other neuronal compartments including GABAergic and glutamatergic synapses as a homeostatic feedback mechanism. Moreover, a coupling of extracellular ion concentrations to a large glial–vascular bath can take a role as an inhibitory mechanism crucial in ion homeostasis (Hübel et al. 2014).

### *C. Interactions between neuronal and hemodynamics responses to tDCS perturbation towards homeostatic regulation of neuronal excitability*

Homeostatic regulation of neuronal excitability refers to the collective phenomena by which neurons alter their intrinsic or synaptic properties to maintain a target level of electrical activity (Williams et al. 2013). This can be abstractly represented as feedback control, e.g., in homeostatic plasticity, where model neurons with activity-dependent maximal conductances can modify their conductances to maintain a given behavior when perturbed (LeMasson et al. 1993). Homeostatic plasticity suggests that the ease with which a synaptic connection is facilitated/suppressed depends on the previous amount of network activity (Müller et al. 2007) (Siebner et al. 2004)(Lang et al. 2004) (Fricke et al. 2011). Fricke and coworkers (Fricke et al. 2011) hypothesized the role of L-type voltage-gated Ca2+ channels (L-VGCC) in short-term homeostatic plasticity, since tDCS has been shown to induce a long-lasting disturbance of Ca2+ homeostasis (Islam et al. 1995) and induce calcium-dependent plasticity (Nitsche et al. 2003). The aftereffects of tDCS have been shown to depend on the modulation of both GABAergic and glutamatergic synapses (Stagg and Nitsche 2011). For example (Fricke et al. 2011), five-minute anodal tDCS increases motor cortex excitability for about 5 min while the cathodal tDCS of

the same duration reduces excitability. Increasing the duration of tDCS to 10 min prolongs the duration of the effects, and if the two 5-min periods of tDCS were applied with a 30-min break between them, then the effect of the second period of tDCS was identical to that of the 5-min stimulation alone. However, if the break is only 3 min, then the second session had the opposite effect to 5-min tDCS given alone. Here, LTP/LTD can be elicited by activating N-methyl-d-aspartate (NMDA)-type glutamate receptors, typically by the coincident activity of pre- and postsynaptic neurons (Lüscher and Malenka 2012). Fricke and coworkers (Fricke et al. 2011) proposed two ideas based on prior animal experiments (see (Turrigiano 2008)(Malenka and Bear 2004)): 1) that the direction [long-term potentiation (LTP)/long-term depression (LTD)] of synaptic plasticity depends on the magnitude and dynamics of different postsynaptic levels of Ca2+ induced by the presynaptic input, with high levels favoring LTP and lower levels LTD; and 2) that the history of activation of a neuron can affect the function of L-VGCC channels such that high preceding levels of activity would reduce their activity, whereas low levels would increase it. Moreover, neuronal activity can trigger Ca2+ signals (Islam et al. 1995) in apposed glial cells and glial Ca2+ waves can affect neurons (Verkhratsky et al. 1998) where the glial network may have an important role (i.e., spatial buffering) in regulating neural activity by distributing the ions (Halnes et al. 2013). Here, an influence of the long-lasting disturbance of Ca2+ homeostasis on the myogenic and the metabolic control of cerebral circulation cannot be excluded.

Furthermore, depolarization of presynaptic glutamate terminals can increase the probability of glutamate release, and the glutamate uptake into astrocytes may stimulate aerobic glycolysis - a mechanism coupling neuronal activity to glucose utilization (Pellerin and Magistretti 1994). Moreover, the spontaneous firing rate (Radman et al. 2009) causing an increase in extracellular potassium concentration will result in concomitant change in intracellular chloride concentration via potassium-coupled chloride cotransport. The action of GABA is primarily determined by the concentration of intracellular chloride (DeFazio et al. 2000). Also, extracellular potassium ions are a direct mediator of vasodilation (Eckman and Nelson 2001). Moreover, glutamate released into the synapse can facilitate astrocyte-mediated vasodilation. Due to vessel dilation, the rates of glucose flux transfer across the endothelium into the interstitium increases. Consequently, astrocytes and neurons may uptake glucose (and lactate) from the interstitium to fuel recovery/maintenance of homeostasis during/following tDCS (Hübel et al. 2014). Indeed, recent work showed that lactate can modulate the activity of primary

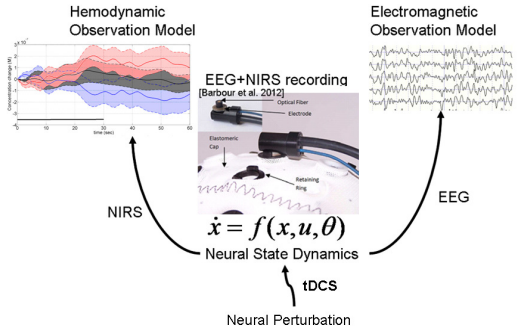


Figure 1.2: EEG-NIRS monitoring of hemodynamic and electromagnetic responses evoked with tDCS (Dutta 2014)

cortical neurons through a receptor-mediated pathway (Bozzo et al. 2013) and vasomotion rhythms can influence neural firing patterns (Nikulin et al. 2014). Moreover, lactate promotes plasticity gene expression by potentiating NMDA signaling in neurons where the action of lactate is mediated by the modulation of NMDA receptor activity (Yang et al. 2014). Therefore, it was postulated that the interactions between neuronal and hemodynamics responses, i.e. the neurovascular coupling functionality, is directed towards homeostatic regulation of neuronal excitability during/following tDCS in the healthy brain. Chander and Chakravarthy (Chander and Chakravarthy 2012) presented a computational model (see Figure 1.1) that studied the effect of metabolic feedback on neuronal activity to bridge the gap between measured hemodynamic response and ongoing neural activity where hemodynamic response is often conceptualized as a unidirectional influence, arising from neurons and acting on vessels. Here, the function of the neurovascular unit (NVU) consisting of the endothelium, glia, neurons, pericytes, and the basal lamina is to maintain the homeostasis of the brain microenvironment (Iadecola 2004) in which neurons, astrocytes, and vessels are semi-independent networks operating in tandem. Here, this unexpected role of lactate as a signaling molecule was found recently (Yang et al. 2014), which lends to our hypothesis that the possibility of (delayed) “reverse” influence in the NVU from the vessel back to neuron via lactate (see Figure 1.1 (Chander and Chakravarthy 2012)) may at least partially explain the time course of the induction of homeostatic plasticity generated by repeated tDCS of the human motor cortex.

Based on these prior works, we recently proposed EEG-NIRS-based (see Figure 1.2) screening and monitoring of neurovascular coupling functionality under perturbation with tDCS (Dutta 2014) where these neuronal and hemodynamics responses can be abstractly represented as feedback control. Here, system identification and parameter estimation techniques (e.g. ARX models (Ljung 1999)) can be used to identify the input-output behavior of the NVU. The objective of this thesis was to assess the feasibility of this concept with,

1. design and development of low-cost instrumentation for the stroke study in India, presented in Chapter 2.
2. methods towards validation of the low-cost instrumentation through a stroke study in India, presented in Chapter 3.
3. results from exploration of neurovascular coupling using perturbation with tDCS in stroke survivors, presented in Chapter 4.
4. discussion of the relevance of our preliminary results and the proposed future work, presented in Chapter 5.

# Chapter 2 - Instrumentation Development

## *A. Development of a low-cost continuous wave NIRS hardware*

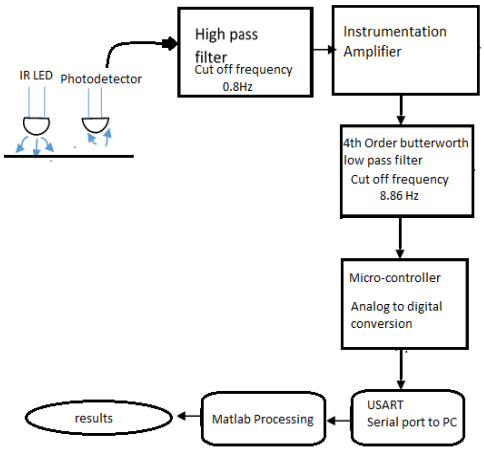


Figure 2.1: NIRS monitoring of hemodynamic responses evoked with tDCS (Sood et al. 2014).

Near-infrared spectroscopy (NIRS) is a cerebral monitoring method that noninvasively and continuously measures cerebral hemoglobin oxygenation which is widely used for monitoring of cerebral vascular status under various clinical conditions. The photons in the near-infrared (NIR) spectral range (650–950 nm) are able to penetrate human tissue. NIR wavelengths can be selected such that the change in concentration of oxy-hemoglobin ($HbO2$) and deoxy-hemoglobin ($Hb$) in the brain tissue can be detected. NIRS instrumentation works on different measuring principles, e.g., continuous wave (CW), frequency domain (FD), and time domain (TD). Absolute concentration measurements may be possible with more expensive TD and FD techniques (Scholkmann et al. 2014) but quantification was not a crucial factor in our application, since we wanted to detect a relative change in $HbO2$ and $Hb$ in response to tDCS rather than to quantify the hemodynamic response in absolute terms. Therefore, we aimed to develop a 4-channel low-cost CW NIRS system that captures the hemodynamic changes during anodal tDCS (Sood et al. 2014). The wavelengths used were 770nm and 850nm, and the distance between the source and the detector was kept at 2.5cm. The signal obtained at the 4 channels was high pass filtered ($freq_{cutoff}$ = 0.8Hz) and amplified by an instrumentation amplifier followed by a fourth order Butterworth low pass filter ($freq_{cutoff}$ = 8.86Hz). The block diagram of the setup is shown in Figure 2.1. Differential spectroscopy has been used to obtain relative changes in the concentrations of the two chromophores, viz. oxy-hemoglobin ($HbO2$) and deoxy-hemoglobin ($Hb$) (Scholkmann et al. 2014). The modified Beer Lambert Law was used to relate the chromophore concentration to the optical absorption values to estimate the differential oxyhemoglobin and deoxyhemoglobin concentrations. This 4-channel low-cost CW NIRS system costs roughly $500 (Sood et al. 2014). For multi-channel approaches required for whole head measurements, a custom-made CW NIRS system

based on an off-the-shelf data acquisition (DAQ) device to interface between signal and computer may provide the user with a robust, fast and flexible solution (Soraghan et al. 2008). A multifunction off-the-shelf DAQ device (National Instruments Corporation, USA) can be used to provide basic physical input/output channels to drive the light sources and/or acquire optical signals. If timing accuracy of DAQ is critical, e.g. for cross spectral analysis (Anirban Dutta 2014a), then a real-time off-the-shelf DAQ system, such as CompactRIO or PXI (National Instruments Corporation, USA), is required. Usually, the number of analog output channels are limited in off-the-shelf DAQ devices (e.g., only 2 analog outputs in PCIe-6351 from National Instruments Corporation, USA) and therefore the time division multiplexing technique can be used to illuminate multiple light sources (light emitting diodes or laser diodes). For example, the NIR light sources can be amplitude-modulated at different carrier frequencies with a gap (viz. 2 to 4 KHz in steps of 200Hz) using a driving circuit that includes a multiplexer and driver for the laser diode (LD) or light emitting diode (LED) to emit NIR light in consecutive time slots. LED, which emit incoherent and uncollimated light, is preferred since it allows the emission of more NIR photons into the tissue than LD with the same maximum permissible exposure (Soraghan et al. 2008). Dual-wavelength LEDs can be used instead of two separate LEDs (as in our 4-channel low-cost CW NIRS system, Figure 2.2a) in a multi-channel high density whole head system. Moreover, an individual programmable current source for each LED can be used so that the emitted light can be automatically adapted to variable individual acquisition conditions (hair, skin color, different tissue types such as muscle, brain etc. as well as a possible effect of EEG gel on the optical properties of the light path) (Safaie et al. 2013). Then, the backscattered NIR light can be collected (light collected is usually 7 to 9 orders smaller in magnitude than that emitted at the source (Lareau et al. 2011)) and converted into an electrical signal by photodiodes. Due to low signal to noise ratio (SNR) of the output signal from the photodiodes, the signal can be band-pass filtered and amplified to increase the SNR. A programmable gain amplifier (e.g. PGA204, Texas Instruments Inc., USA) can be used to adapt the gain depending on source-detector distance, scalp thickness, and hair color and density (Scholkmann et al. 2014) to match the voltage range of the analog input channel of the DAQ device. This custom-made whole head CW NIRS system based on an off-the-shelf DAQ device is under development and the design documents will be available at https://team.inria.fr/nphys4nrehab/hardware/

### *B. Development of a low-cost tDCS hardware*

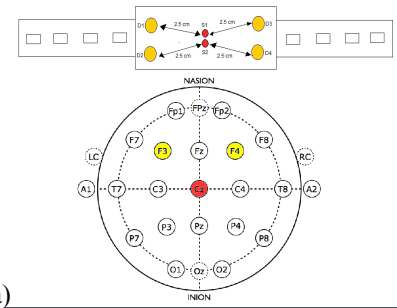


a)

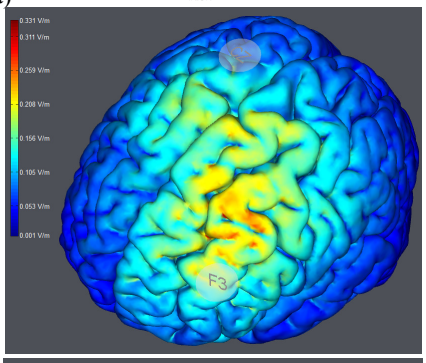


b)

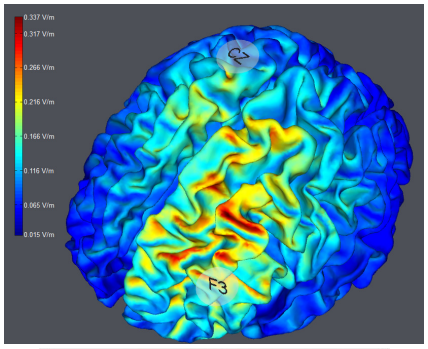


c)

d)

Figure 2.2: a) Top panel: NIRS detectors (D), and 770nm and 850nm sources (S). Bottom panel: tDCS scalp sites where red denotes the anodal and yellow denotes the cathodal tDCS electrodes. b) Electric field magnitude in the grey matter due to F3 cathodal and Cz anodal tDCS, c) Electric field magnitude in the white matter due to F3 cathodal and Cz anodal tDCS, d) Patient studies conducted at the Institute of Neurosciences Kolkata, India.

The low-cost tDCS hardware is based on a current regulator that sets and stabilizes the current at a fixed level. The current was controlled using a three terminal adjustable current source (LM334Z, Texas Instruments, USA) - featuring 10,000:1 range in operating current, excellent current regulation and a wide dynamic voltage range of 1V to 40V - where the current level was set with one external resistor, i.e., an analog potentiometer (Sood et al. 2014). The low-cost tDCS hardware was capable of providing a constant current ranging from 0.25mA to 2.25mA with an initial current accuracy of ±3% (Sood et al. 2014). A bypass capacitor was used across the anode and cathode of the low-cost tDCS hardware to dampen the noise. The ramp up (30sec), ramp down (30sec), and the constant current level that are usually parts of tDCS protocol were achieved with a digital potentiometer. The low-cost tDCS hardware allowed adjustment of output current in fine increments (i.e., 0.1 or 0.25mA steps). The tDCS was delivered to the scalp using conductive rubber electrodes covered with saline soaked sponge in a conventional montage (Nitsche and Paulus 2000). This tDCS hardware costs roughly $100 in parts (Sood et al. 2014). The focality of tDCS may be improved with a high definition montage (Edwards et al. 2013) (Kuo et al. 2013) or other optimized multi-electrode configurations (Dmochowski et al. 2011). Therefore, a programmable multi-channel stimulator is under development for current steering using multiple independent current sources (current regulators) to independently target different cerebral outer convex vascular territories. The design documents will be available at https://team.inria.fr/nphys4nrehab/hardware/

## Chapter 3 - Methods for the Stroke Pilot Studies

### *A. Experiments 1: stroke study using the low-cost NIRS-tDCS hardware*

After bench testing on healthy subjects, 14 patients with established and subacute ischemic stroke (<1 month) restricted to a single hemisphere (10 male and 4 females between age 42 to 73) were recruited for clinical validation. Subjects were recruited after ethics approval and experiments were conducted at the Institute of Neurosciences Kolkata, India after taking informed consent, conforming to the Declaration of Helsinki. Participants were seated in a quiet room and their eyes were open and fixed on a point on the wall in front of them during the entire experiment. The total testing time was roughly 14 minutes. Anodal tDCS with the anode positioned at Cz (international 10-20 system of scalp sites) and the cathode over F3 (F4 when monitoring the right side) was conducted with a current density maintained at 0.526A/m$^2$ (see Figure 2.2). This F3 (F4 when monitoring the right side) cathodal and Cz anodal tDCS montage was selected based on computational modeling (using StimViewer, Neuroelectrics, Spain)(Miranda et al. 2013) in order to target primarily the outer convex brain territory (superficial divisions) of the middle cerebral artery (MCA). MCA is one of the three major paired arteries that supply blood to the cerebrum and is the most common site of stroke. Figure 2.2 b and c show the electric field magnitude in the grey matter and the white matter respectively due to F3-Cz tDCS montage. The low-cost continuous wave NIRS hardware consisted of four detection channels (see Figure 2.2a) that was placed on either F3 (for F3-Cz tDCS montage) or F4 (for F4-Cz tDCS montage) site (see Figure 2.2a). In our subjects with ischemic stroke (<1 month) restricted to a single hemisphere, the montages (F3-Cz or F4-Cz) were selected to target the ipsilesional and contralesional hemisphere in separate sessions, with the order randomized across subjects. For example, Figure 2.2d shows a patient study. Here, NIRS was performed for two minutes on the lesioned hemisphere followed by tDCS for three minutes with a montage targeting the lesioned hemisphere. After tDCS that targeted mostly the lesioned hemisphere, NIRS was performed again on the lesioned hemisphere to measure any change due to tDCS. The percent change in HbO2 ($\%\Delta HbO2$) post-tDCS from pre-tDCS baseline were compared using paired-sample t-test.

$$\%\Delta HbO2 = \frac{HbO2_{post-tDCS} - HbO2_{pre-tDCS}}{HbO2_{post-tDCS} + HbO2_{pre-tDCS}}$$

The same process was repeated with the contralesional hemisphere to find differences (lesional versus contralesional) in the NIRS response since ischemic stroke was restricted to a single hemisphere.

During tDCS-facilitated cortical neural activity, the electric currents from all excitable membranes of brain tissue superimpose at a given location in the extracellular medium and generate a potential, which is referred to as the electroencephalogram (EEG) when recorded from the scalp (Buzsáki et al. 2012). Quantitative EEG analysis has been used as a method of identifying subclinical brain injury during neurosurgical procedures, such as carotid endarterectomy, and for ischemia detection, global function assessment, medication titration, and prognostication (Foreman and Claassen 2012). Furthermore, EEG parameters could reliably discriminate between stroke and transient ischaemic attack (TIA) patients or control subjects, and correlated significantly with clinical and radiological status with high multilevel reproducibility (Sheorajpanday et al. 2009). Therefore, reliable EEG parameters can be evaluated in a general stroke population for clinically relevant state and outcome measures (Sheorajpanday et al. 2009). Several studies investigated the relationship between EEG alpha rhythm variations (alpha rhythm lies in the range of 8 to 13 Hz) and baseline regional CBF differences (Jann et al. 2010). The hemodynamic responses associated with cortical neural activity, i.e., the relationship between local neural activity and cerebral blood flow is termed neurovascular coupling (NVC) (Filosa 2010). Therefore, EEG may provide a measure that is independent from NIRS measure where simultaneous EEG-NIRS imaging (Barbour et al. 2012)(Safaie et al. 2013) during perturbation with tDCS may help us to understand the NVC underlying neural and hemodynamic responses post-stroke. Furthermore, EEG-NIRS joint imaging may improve the specificity by estimating NVC as a biomarker for post-stroke impaired cerebral microvessels functionality (see Figure 1) (Dutta 2014) where non-neuronal systemic physiological fluctuations often contaminate NIRS signals. The next objective was a proof-of-concept study on EEG-NIRS imaging using off-the-shelf EEG-tDCS and NIRS devices.

### *B. Experiments 2: stroke case series using off-the-shelf EEG-tDCS and NIRS devices*

Simultaneous recording of NIRS and EEG (Barbour et al. 2012) during anodal tDCS was conducted on four chronic (>6 months, see Table 2.1) ischemic stroke survivors after obtaining informed consent.

All experiments were conducted in accordance with the Declaration of Helsinki at the Neuro Rehab Services LLP, India.

Table 2.1: Summary of the case series (M: male, F: female, MCA: middle cerebral artery, CABG: coronary artery bypass graft).

| Case | Age/gender | MRI diagnosis | Comorbidities | Year of stroke |
|---|---|---|---|---|
| 1 | 31/M | Right MCA stroke | None | 2008 |
| 2 | 63/M | Left MCA stroke | Diabetis, Hypertension | 2009 |
| 3 | 73/M | Left MCA stroke | Post-CABG | 2010 |
| 4 | 76/F | Right MCA stroke | Post-CABG | 2009 |

The tDCS (StarStim, Neuroelectrics, Spain) was conducted with the anode (SPONSTIM-8, Neuroelectrics, Spain) placed at Cz (international 10-20 system of scalp sites) and the cathode (SPONSTIM-25, Neuroelectrics, Spain) over left supraorbital notch with a current density of $0.526A/m^2$. The tDCS was turned ON for 30sec and then OFF for 30sec, which was repeated 15 times. Eyes-open block-averaged resting-state NIRS was conducted at the central site Cz by inserting 1 source (760/850nm LED) through the $8cm^2$ sponge (rubber core electrode) and with 4 symmetrically-placed detectors at 2.5 cm source-detector separation. NIRS (NIRx, USA) was recorded at 22.5Hz using a spatially resolved spectroscopy technique (Choi et al. 2004) and then pre-processed using HomER functions (Huppert et al. 2009). Also, eyes-open resting state EEG (StarStim, Neuroelectrics, Spain) was recorded at 500Hz from the nearby electrodes F3, F4, P3, P4 (international 10-20 system), which were interpolated with spherical splines to estimate the EEG at Cz (virtual electrode) using EEGLAB 'eeg_interp()' function (Delorme and Makeig 2004). The EEG at the central site Cz (virtual electrode) before and immediately after anodal tDCS at Cz was pre-processed using EEGLAB functions (Delorme and Makeig 2004).

### *C. EEG-NIRS imaging based assessment of neurovascular coupling under tDCS perturbation*

Prior work has shown that tDCS induces changes in neuronal membrane potentials in a polarity-dependent manner and induces synaptically driven after-effects after a sufficient duration (Molaee-Ardekani et al. 2013). Basal and apical dendrites can be concomitantly polarized in opposite directions (Rahman et al. 2013). Consequently stimulation results in local excitatory (or, inhibitory) postsynaptic current, which then results in an excitatory (or, inhibitory) postsynaptic potential at the cell body

causing respective membrane potential alterations. The synaptic transmembrane currents are a major contributor of the extracellular signal that can be measured with current source density (CSD) analysis of the extracellular field potentials, viz., local field potentials (LFP) (Buzsáki et al. 2012). EEG monitors the extracellular field potentials which can be used to estimate the EEG surface laplacian (Carvalhaes and Suppes 2011) - the magnitude of the radial (transcranial) current flow leaving (sinks) and entering (sources) the scalp. These reference-free CSD waveforms yield measures that closely represent underlying neuronal current generators (Perrin et al. 1989), and therefore CSD waveforms at the site of stimulation, Cz, should represent underlying neuronal current generators. Prior work shows a strong coupling between LFP and regional vascular responses even in the absence of spikes (i.e., sub-threshold depolarization) (Viswanathan and Freeman 2007). Moreover, our prior work showed an increase of fractional power in the Theta band (4-8Hz) and decrease around "individual alpha frequency" in the Alpha band (8-13Hz) following anodal tDCS (Anirban Dutta 2013). In this study, NIRS complemented the electrophysiological measures with measurements of the changes in (cortical) tissue oxy-( $HbO2$ ), and deoxy-( $Hb$ ) hemoglobin concentration roughly underlying Cz location. Total hemoglobin concentration, $Hbt$ , is considered as a good indicator of variations in regional cerebral blood volume (Villringer and Chance 1997) which was derived as the sum of $HbO2$ and $Hb$ concentrations.

After pre-processing EEG in EEGLAB (Delorme and Makeig 2004), Empirical Mode Decomposition (EMD) into a set of intrinsic mode functions ($IMF_{EEG}$) was performed using the Hilbert-Huang Transform (HHT) (Huang et al. 1998). Also, NIRS-measured changes in (cortical) tissue oxy-( $HbO2$ ), and deoxy-( $Hb$ ) hemoglobin concentration in the volume roughly underlying the Cz location, which was pre-processed in HomER (Huppert et al. 2009). After pre-processing, Empirical Mode Decomposition (EMD) into a set of intrinsic mode functions ($IMF_{NIRS}$) was performed on the $HbO2$ time-series. Resting-state neurovascular coupling from EEG-NIRS recordings was assessed as follows.

1. Empirical Mode Decomposition (EMD) of non-stationary electrophysiological and hemodynamic resting-state time-series into a set of intrinsic mode functions (IMFs) using the Hilbert-Huang Transform (HHT) (Huang et al. 1998). Generally, the first IMF contains the highest frequency

components and the oscillatory frequencies decrease with increasing IMF index. The IMFs for EEG are denoted as $IMF_{EEG}$ and IMFs for $HbO2$ are denoted as $IMF_{NIRS}$.

2. Then, the cross correlation function between the $IMF_{NIRS}$ and log-transformed mean-power time-series (non-overlapping 2 seconds moving window) of $IMF_{EEG}$ was obtained using MATLAB toolbox (Zhou et al. 2009). The component of $IMF_{NIRS}$ and $IMF_{EEG}$ that optimally represented the non-stationary effects of anodal tDCS was used for the assessment of neurovascular coupling.

3. For the assessment of neurovascular coupling (NVC) during anodal tDCS from the non-stationary $IMF_{NIRS}$ and $IMF_{EEG}$ components, the Hilbert transform of the $IMF_{NIRS}$ and log-transformed mean-power time-series of $IMF_{EEG}$ ($PIMF_{EEG}$) was first performed,

$$H_{EEG,i}(t) = \frac{1}{\pi} P \int_{-\infty}^{\infty} \frac{PIMF_{EEG,i}(\tau)}{t-\tau} d\tau$$
$$H_{NIRS,i}(t) = \frac{1}{\pi} P \int_{-\infty}^{\infty} \frac{IMF_{NIRS,i}(\tau)}{t-\tau} d\tau \quad (1)$$

where $P$ is the Cauchy principal value. Then, the analytic signals were defined as,

$$Z_{EEG,i}(t) = PIMF_{EEG,i}(t) + iH_{EEG,i}(t)$$
$$Z_{NIRS,i}(t) = IMF_{NIRS,i}(t) + iH_{NIRS,i}(t) \quad (2)$$

The instantaneous amplitudes for the analytic signals were determined as,

$$A_{EEG,i}(t) = \left[ PIMF^2_{EEG,i}(t) + H^2_{EEG,i}(t) \right]^{1/2}$$
$$A_{NIRS,i}(t) = \left[ IMF^2_{NIRS,i}(t) + H^2_{NIRS,i}(t) \right]^{1/2} \quad (3)$$

The instantaneous phases for the analytic signals were determined as,

$$\theta_{EEG,i}(t) = \arctan\left( \frac{H_{EEG,i}(t)}{PIMF_{EEG,i}(t)} \right)$$
$$\theta_{NIRS,i}(t) = \arctan\left( \frac{H_{NIRS,i}(t)}{IMF_{NIRS,i}(t)} \right) \quad (4)$$

The instantaneous frequency for the analytic signals was determined as,

$$f_{EEG,i}(t)=\frac{1}{2\pi}\frac{d\theta_{EEG,i}(t)}{dt}$$
$$f_{NIRS,i}(t)=\frac{1}{2\pi}\frac{d\theta_{NIRS,i}(t)}{dt} \quad (5)$$

To compute cross-spectrum and coherence during anodal tDCS for the assessment of NVC, the component of $IMF_{NIRS}$ and $IMF_{EEG}$ that best represented the non-stationary effects of anodal tDCS were selected (say, $IMF_{NIRS,j}(t)$ and $PIMF_{EEG,k}(t)$) for further analysis.

4. The cross-spectrum and coherence between $PIMF_{EEG,k}(t)$ and $IMF_{NIRS,j}(t)$ during anodal tDCS were calculated based on their instantaneous amplitude and phase. Here, a moving window method was followed where the average instantaneous frequency was first computed. Then, the cross-spectrum at time instant, $t$, was computed for the frequency, $f_p$, from $m^{th}$ and $n^{th}$ observation windows (i.e., $PIMF_{EEG,k,m}(t)$ and $IMF_{NIRS,j,n}(t)$) which have average instantaneous frequency closest to $f_p$, i.e.,

$$C_{f_p}(PIMF_{EEG,k},IMF_{NIRS,j})=A_{EEG,k,m}(t)A_{NIRS,j,n}(t)e^{i\left[\theta_{EEG,k,m}(t)-\theta_{NIRS,j,n}(t)\right]}$$
$$C_{f_p}(IMF_{NIRS,j},PIMF_{EEG,k})=A_{NIRS,j,n}(t)A_{EEG,k,m}(t)e^{i\left[\theta_{NIRS,j,n}(t)-\theta_{EEG,k,m}(t)\right]} \quad (6)$$

Also, the coherence was computed as,

$$Coh_{EEG\rightarrow NIRS,f_p}=\frac{\left\langle C_{f_p}(PIMF_{EEG,k},IMF_{NIRS,j})^2\right\rangle}{\left\langle\left[A_{EEG,k,m}(t)e^{i\theta_{EEG,k,m}(t)}\right]^2\right\rangle\left\langle\left[A_{NIRS,j,n}(t)e^{i\theta_{NIRS,j,n}(t)}\right]^2\right\rangle} \quad (7)$$

$$Coh_{NIRS\rightarrow EEG,f_p}=\frac{\left\langle C_{f_p}(IMF_{NIRS,j},PIMF_{EEG,k})^2\right\rangle}{\left\langle\left[A_{NIRS,j,n}(t)e^{i\theta_{NIRS,j,n}(t)}\right]^2\right\rangle\left\langle\left[A_{EEG,k,m}(t)e^{i\theta_{EEG,k,m}(t)}\right]^2\right\rangle}$$

where $\langle\ \rangle$ denotes averaging over multiple paired-windows for the given frequency, $f_p$. Significant positive values point to a causal relation (Dhamala et al. 2008).

5. The mean neurovascular coupling (NVC) for a given frequency range, $\Delta f_p$ ,.was defined as,

$$NVC_{EEG\rightarrow NIRS}(\Delta f_p) = \left\langle Coh_{EEG\rightarrow NIRS,f_p} \right\rangle$$
$$NVC_{NIRS\rightarrow EEG}(\Delta f_p) = \left\langle Coh_{NIRS\rightarrow EEG,f_p} \right\rangle \quad (8)$$

where $\langle\ \rangle$ denotes averaging over a given frequency range, $\Delta f_p$, over all the trials.

All computations were performed with custom-code developed in Matlab R2011a (The Mathworks Inc, USA).

## Chapter 4 - Results from the Stroke Pilot Studies

### *A. Results 1: stroke study using the low-cost NIRS-tDCS hardware*

The affected hemisphere of the brain with impaired circulation showed significantly less increase (and mostly decrease) in cerebral oxygen saturation as compared to non-lesioned side in response to anodal tDCS. There was significant change in cerebral oxygen saturation post-tDCS from pre-tDCS baseline in the non-lesioned side (3.43 ± 0.86) but not in the lesioned side (0.26 ± 0.28), $p<0.01$ (Sood et al. 2014). Figure 4.1 shows the scatter plot of $\%\Delta HbO2$ (i.e., percent change in $HbO2$ post-tDCS from pre-tDCS value) by group - left hemispheric (side) stroke, right hemispheric (side) stroke.

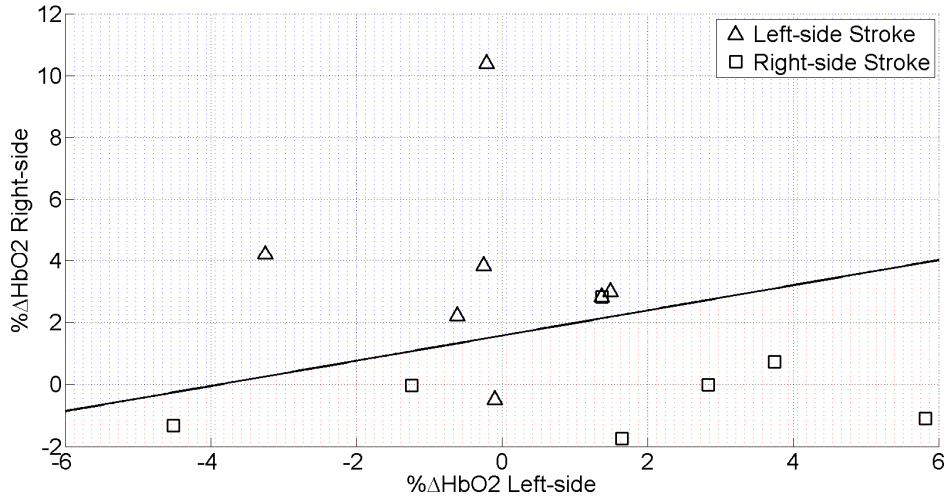


Figure 4.1: The scatter plot of $\%\Delta HbO2$ (i.e., percent change in $HbO2$ post-tDCS from pre-tDCS value) by group (N=14) - left side stroke, right side stroke.

### *B. Results 2: stroke case series using off-the-shelf EEG-tDCS and NIRS devices*

The illustrative results from Case-1 are shown in Figure 4.2, where the top-panel of Figure 4.2a shows the regional change in tissue oxy- ($HbO2$), deoxy- ($Hb$), and total ($Hbt$) hemoglobin concentration from 0-60sec due to application of 0.526A/m$^2$ anodal tDCS from 0-30sec. The 8th intrinsic mode function (IMF-8) mostly captured the temporal change in $HbO2$ that represent non-stationary effects of anodal tDCS including the initial dip, as shown in the bottom panel of Figure 4.2a. The duration of this initial dip was computed from the IMF-8 time-series for each trial for all subjects (4 subjects, 15 trials each). The initial dip-duration for Case-1 (12.13±3.81sec) was much longer than those of the other three cases (6.04±3.82sec). The corresponding EEG spectrogram for Case-1 using short-time Fourier transform for the interpolated EEG estimate at Cz (virtual electrode) is shown in the

top

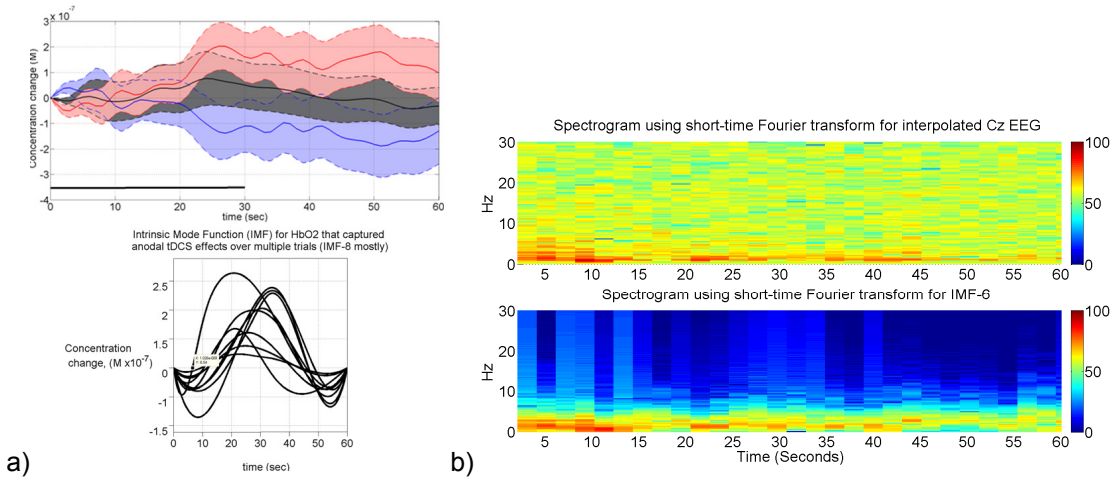


a) b)

Figure 4.2: Case-1 results. a) Top Panel: Regional change in tissue oxy- ($HbO2$ in red), deoxy- ($Hb$ in blue), and total ($Hbt$ in grey) hemoglobin concentration from 0-60sec due to application of 0.526A/m$^2$ anodal tDCS from 0-30sec. Bottom Panel: The 8th intrinsic mode function (IMF-8) captured the temporal change in $HbO2$ including an initial dip. b) Top Panel: Spectrogram showing non-stationary single-trial EEG (interpolated at Cz) during anodal tDCS. Bottom Panel: The 6th intrinsic mode function (IMF-6) primarily captured the temporal change in the power spectral density.

panel of Figure 4.2b. Here, the 6th intrinsic mode function (IMF-6) mostly captured the non-stationary effects of anodal tDCS on the power spectral density (PSD) within the 0.5Hz-11.25Hz frequency band, which is shown in the bottom panel of Figure 4.2b. Therefore, IMF-8 for $HbO2$ and IMF-6 for interpolated EEG at Cz (virtual electrode) were selected for the assessment of neurovascular coupling (NVC) during anodal tDCS. We investigated NVC during tDCS, assuming that anodal tDCS facilitated cortical neural activity, resulting in glutamate release into the synapse, and consequently facilitating astrocyte-mediated vasodilation, which was assessed with $NVC_{EEG\rightarrow NIRS}(0.5\text{Hz-}11.25\text{Hz})$.

Figure 4.3a compares the log-transformed mean-power of IMF-6 with the log-transformed mean-power of EEG (interpolated at Cz) within 0.5Hz-11.25Hz. It was found that log-transformed mean-power time-series of IMF-6 captured the log-transformed mean-power time-course of the EEG (interpolated at Cz) within 0.5Hz-11.25Hz, showing non-stationary effects of anodal tDCS (see Figure 4.2b). Figure 4.3b shows the cross-correlation function between the IMF-8 of $HbO2$ (Figure 4.2a) and the log-transformed mean-power time-series of IMF-6 (Figure 4.2b). Here, a negative cross correlation of ~0.6 with a zero lag (95 percent confidence interval) was found for this trial during anodal tDCS. Figure 4.3c shows the cross-correlation function between the IMF-8 of $HbO2$ (Figure 4.2a) and the log-transformed mean-power time-series of IMF-6 (Figure 4.2b) during post-tDCS resting-state (i.e., no task and no tDCS), which was found to be positive ~0.6 with a lead of 5sec (95 percent confidence

interval).The results including the $NVC_{EEG\rightarrow NIRS}(0.5\text{Hz-}11.25\text{Hz})$ during anodal tDCS from all the trials (N=15) for all four cases are listed in Table 4.1.

Table 4.1: Summary of the results from the case series.

| Case | During tDCS (mean±1 std. dev.) | | | Post-tDCS (mean±1 std. dev.) | |
|---|---|---|---|---|---|
| Trials (N=15) | Correlation Coefficient | $NVC_{EEG\rightarrow NIRS}(0.5\text{Hz-}11.25\text{Hz})$ | Lag (sec) | Correlation Coefficient | Lag (sec) |
| 1 | -0.56±0.21 | 0.93 | 0.93±1.26 | 0.57±0.16 | -5.19±1.42 |
| 2 | -0.64±0.15 | 0.81 | 3.28±1.38 | 0.62±0.19 | -4.75±1.57 |
| 3 | -0.58±0.13 | 0.79 | 2.75±1.96 | 0.59±0.18 | -6.09±1.29 |
| 4 | -0.55±0.19 | 0.78 | 3.56±1.19 | 0.58±0.12 | -6.18±1.17 |

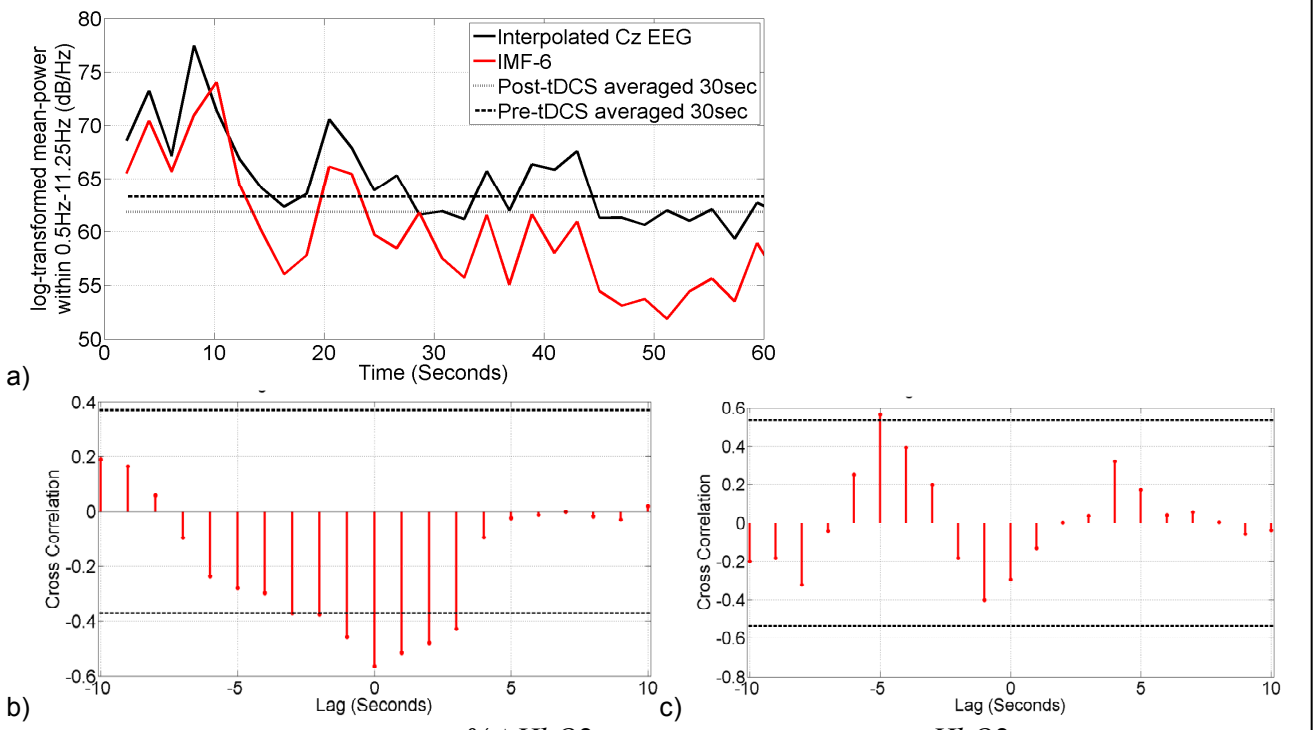


Figure 4.3: a) The scatter plot of $\%\Delta HbO2$ (i.e., percent change in $HbO2$ post-tDCS from pre-tDCS value) by group (N=14) - left side stroke, right side stroke. b) Case-1 results: the 6th Intrinsic Mode Function (IMF-6) of the interpolated EEG estimate at Cz (virtual electrode) captured the temporal change in the log-transformed mean-power (within 0.5Hz-11.25Hz) of the EEG. c) Case-1 results: Cross-correlation function during anodal tDCS between log-transformed mean-power time-course of $IMF_{EEG}$ and $IMF_{HbO2}$ time-series. d) Case-1 results: Cross-correlation function during post-tDCS resting-state (i.e., no task/no tDCS) between log-transformed mean-power time-course of $IMF_{EEG}$ and $IMF_{HbO2}$ time-series. In c) and d), dashed lines show 95 percent confidence interval for the assumption that the two time series are completely uncorrelated.

## Chapter 5 - Discussion and Future Work

With the low-cost NIRS-tDCS device, it was possible to conduct transcranial cerebral oximetry, i.e. a non-invasive point-of-care technique to measure changes in regional cerebral oxygen saturation following tDCS (Sood et al. 2014). NIRS monitored oxygen saturation of hemoglobin in the entire tissue bed, which includes a mixture of brain tissue, arterial and venous blood. To understand the mechanisms underlying NIRS responses elicited by tDCS, we proposed a phenomological model (based on the Friston model) (Dutta et al. 2013). It was assumed that anodal tDCS causes changes in synaptic transmembrane current, resulting in change in CBF via a change in the representative radius of the vasculature, and not in arterial and venous blood pressure difference. Furthermore, it was assumed in the phenomological model that the changes from baseline in the NIRS recording of oxygen saturation during tDCS were solely due to the local hemodynamic effects (mainly venous blood) induced by tDCS and not due to changes in arterial oxygen concentration. Also, we assumed that the spatially resolved spectroscopy technique removed skin blood flow artifacts from the NIRS signal, but this needs to be verified with a time-gated optical system for depth-resolved NIRS. If needed, short separation NIRS channels can be added to regress out superficial extra-cortical contributions (Gagnon et al. 2012).

### *A. Discussion of study results and limitations*

Our preliminary studies showed the feasibility of identifying the lesioned hemisphere (see Figure 4.1) in subacute stroke with the low-cost NIRS-tDCS hardware (Sood et al. 2014). A significant change in HbO2 post-tDCS from pre-tDCS baseline was found on the non-lesioned side (3.43 ± 0.86) but not in the lesioned side (0.26 ± 0.28), $p<0.01$. In fact, there was mostly a decrease (see Figure 4.1) in cerebral oxygen saturation in response to anodal tDCS in the lesioned side when compared to that in the non-lesioned side. In healthy conditions, cerebral blood flow (CBF) should increase in the brain regions with neural activity (facilitated with anodal tDCS) via metabolic coupling mechanisms whereas the autoregulation mechanisms should ensure that the blood flow is maintained during changes in the perfusion pressure. Therefore, it is postulated that impaired blood flow in the lesioned hemisphere is responsible for a decrease (see Figure 4.1) in cerebral oxygen saturation in response to anodal tDCS in the lesioned side when compared to that in the non-lesioned side in most stroke survivors. However,

it cannot be excluded in certain stroke survivors that the lesioned hemisphere did not respond to anodal tDCS with an increase in neural activity. This might have resulted in an absent change in the cerebral metabolic rate of oxygen, CMRO2 (i.e., oxygen consumption) (Dutta et al. 2013), that is given by the difference of oxygen flowing into and out of the tissue, as compared to the non-lesioned hemisphere. To avoid this problem in our subsequent studies, the effects of tDCS on neural activity was elucidated with simultaneous EEG, which provided an independent measure to supplement NIRS recordings. Based on prior work (Jann et al. 2010) that found an association of individual resting state EEG alpha frequency and cerebral blood flow, we hypothesized that if the changes in EEG during tDCS are correlated with the changes in NIRS then it may enable us to measure the state of the neurovascular coupling. Therefore, a post-stroke case series (4 subjects) using off-the-shelf EEG-tDCS and NIRS hardware was conducted as a proof-of-concept study on EEG-NIRS joint imaging of tDCS effects. Indeed, we found immediate regional changes in tissue oxy- ($HbO2$) and deoxy- ($Hb$) hemoglobin concentration from 0-60sec due to application of 0.526A/m$^2$ anodal tDCS from 0-30sec (Figure 4.2a). Also, non-stationary effects of anodal tDCS on EEG (interpolated at Cz) were identified from the spectrogram, as shown in Figure 4.2b. The results of this case series showed that anodal tDCS induces a local neurovascular response which may be used for assessing regional neurovascular coupling (NVC) functionality. Here, the log-transformed mean-power within 0.5Hz-11.25Hz frequency band was much higher at the beginning (0-10sec) of anodal tDCS when compared to post-tDCS (>30 sec) values in Case-1 (Figure 4.2b). This non-stationary log-transformed mean-power within the 0.5Hz-11.25Hz frequency band was best captured by the 6th intrinsic mode function, IMF-6 (Figure 4.2b). Also, it was found that the 8th intrinsic mode function (IMF-8) mostly captured the non-stationary effects of anodal tDCS on $HbO2$ time-series including the initial dip (12.13±3.81sec in Case-1), as shown in the bottom panel of Figure 4.2a. Therefore, IMF-8 for $HbO2$ and IMF-6 for interpolated EEG at Cz (virtual electrode) were selected for the assessment of neurovascular coupling (NVC) during anodal tDCS, which is summarized in Table 4.1. During anodal tDCS, the negative cross-correlation coefficient was found to be comparable across cases and log-transformed mean-power of IMF-6 for interpolated EEG at Cz (virtual electrode) lagged IMF-8 for $HbO2$. For post-tDCS, the cross-correlation coefficient was positive with a negative lag (i.e., IMF-8 for $HbO2$ lagged log-transformed mean-power of IMF-6 for EEG), which were comparable across subjects. Therefore,

cross-correlation analysis between EEG power and $HbO2$ may elucidate NVC functionality where a clinical study with a higher number of patients is needed for clinical validation. Nevertheless, from our stroke case series, we found that the lag for Case-1 (0.93±1.26sec) differed from the other cases and these alterations lasted longer (12.13±3.81sec dip-duration) for Case-1 than other three cases (6.04±3.82sec). Case-1 was suspected of suffering from small vessel disease (white matter hyperintensities) who also complained of headache with throbbing pain following 15 minutes of anodal tDCS in another study. Indeed, both large intracranial artery stenosis (LIAS) and small vessel disease (SVD) show an uncoupling of the blood supply of active neurons which points to an additional small vessel dysfunction in patients with LIAS (Lin et al. 2011), however, patients with SVD may be more impaired on neurovascular coupling associated with microcirculatory function than patients solely with LIAS. Therefore, an assessment of NVC in addition to CVR can be highly useful for screening and stratification of patients with carotid occlusive disease at a risk of ischemic stroke where a relationship between hemodynamic insufficiency and diminished brain function in the absence of clinically expressed ischemic events can occur (Mikulis 2013).

The major limitation of NIRS is that it provides compositional but not structural information (e.g., as in MRI). Moreover, even though NIRS has advantages (over functional magnetic resonance imaging - fMRI), e.g., a higher temporal resolution (a few ms for NIRS compared to 1-2 seconds for fMRI), relative insensitivity to subject's movements, its cost effectiveness, but the limitation is that it has a lower spatial resolution, and its lack of sensitivity to deeper brain areas (>3 cm of depth). However, lack of NIRS high spatial resolution is not an issue for online imaging of tDCS effects since tDCS focality is also limited (few cm depending on electrode size and montage) (Dmochowski et al. 2011). Furthermore, noninvasive assessment of changes in cytochrome-c oxidase oxidation (energy metabolism) during tDCS may be possible (Heekeren et al. 1999). Here, the advantage of NIRS is its high temporal resolution which when combined with EEG may help us to investigate tDCS mechanisms, e.g., the interactions between neuronal and hemodynamics responses directed towards recovering homeostasis. It has been suggested that a long-lasting disturbance of Ca2+ homeostasis is involved in the cortical plastic changes seen following anodal tDCS (Islam et al. 1995)(Fricke et al. 2011). An influence of long-lasting disturbance of Ca2+ homeostasis on the myogenic and the metabolic control of cerebral circulation cannot be excluded. Also, anodal tDCS might cause a rapid

increase in the extracellular potassium concentration due to outwardly directed potassium currents where diffusing extracellular potassium ions can act as mediators of vasodilation (Eckman and Nelson 2001). Also, diffusing extracellular potassium ions can act on neuronal compartments, including GABAergic and glutamatergic synapses, which may together contribute to the aftereffects of anodal tDCS (Stagg and Nitsche 2011). Moderate rises in the extracellular potassium concentration have been shown to depress high-frequency synaptic transmission (Meeks and Mennerick 2004). Indeed, we found log-transformed mean-power within 0.5Hz-11.25Hz frequency band much higher at the beginning (~0-10sec) of anodal tDCS when compared to post-tDCS (>30 sec) values in Case-1 (Figure 4.2b). Therefore, it can be hypothesized that an immediate response towards recovery of homeostasis was triggered by the extracellular calcium and potassium ions during perturbation with anodal tDCS. This recovery (and maintenance) of homeostasis in the cortex (Hübel et al. 2014) during perturbation by anodal tDCS might be fuelled by glucose (and lactate) uptake by astrocytes and neurons from the interstitium. Subsequent increase in the cerebral metabolic rate of oxygen due to aerobic energy metabolism might have led to a negative cross-correlation between the $HbO2$ time-series and log-transformed mean-power time-course of EEG primarily within 0.5Hz-11.25Hz frequency band (Table 4.1). Here, we postulate that the immediate need to fuel recovery of homeostasis was caused by astrocytes via the lactate shuttle (Pellerin and Magistretti 1994) while blood glucose supply has a longer delay (Gruetter et al. 1996). Therefore, it was hypothesized for Case-1 that the initial (~0-10sec) dip in $HbO2$ at the beginning of anodal tDCS (Figure 4.2a) and corresponding increase in the log-transformed mean-power within the 0.5Hz-11.25Hz frequency band (Figure 4.2b) were related to the recovery of homeostasis. Interestingly, these alterations lasted longer (12.13±3.81sec dip-duration) for Case-1 (suspected of SVD) than other three cases (6.04±3.82sec), and only Case-1 complained about headache after tDCS (Anirban Dutta 2014b). Therefore, this dip-duration in $HbO2$ at the beginning of anodal tDCS that was captured using Intrinsic Mode Function needs to be carefully investigated via longitudinal studies with a higher number of patients to confirm the potential predictive diagnostic value of our CVR and NVC assessments.

### *B. Ongoing and future work*

Arterial atherosclerosis is one of the primary causes of ischemic stroke and with an increasingly aging population, more patients will be diagnosed with large vessel disease (Bos et al. 2014). However, diagnosis and management of arterial atherosclerosis (symptomatic and asymptomatic) poses considerable treatment dilemmas (Lanzino et al. 2009), especially in a low-resource setting. Here, reduced CVR, as a marker of reduced brain vascular reserve, may identify arterial atherosclerosis patients at a higher risk for stroke and vascular dementia (Paraskevas et al. 2014) (Markus and Cullinane 2001). However, the main limitation is the cost, access, and availability of trained technicians and physicians to perform the transcranial doppler (TCD) measurements of CVR (Paraskevas et al. 2014). Therefore, we propose NIRS-EEG/HD-tDCS based CVR (and NVC) assessment that will be validated with measures of cerebral perfusion and CVR (to CO2) by state-of-the-art TCD and arterial spin labeling (ASL) magnetic resonance imaging. Integration of EEG to our low-cost CW NIRS-tDCS device should not increase the cost significantly since low-noise, 8-Channel, 24-Bit Analog Front-End for EEG measurements are available for $200 (ADS1299EEG-FE, Texas Instruments, USA). The design documents will be available at https://team.inria.fr/nphys4nrehab/hardware/

First, the FPGA-based NIRS-EEG/HD-tDCS device will be developed and bench-tested by comparing its recordings with state-of-the-art NIRS, EEG, and tDCS devices via healthy human studies. Then, we will conduct a pilot study on 100 subjects - symptomatic (35 subjects) and asymptomatic carotid stenosis (35 subjects) patients, and age-matched healthy controls (30 subjects) - using the FPGA-based NIRS-EEG/HD-tDCS device where the degree of stenosis will be stratified into categories of normal (no stenosis), <50% stenosis, 50%-69% stenosis, 70%-99% stenosis, near occlusion, and total occlusion based on Society of Radiologists in Ultrasound Consensus Criteria. During the clinical study, the NIRS-EEG/HD-tDCS sensor-electrode will be placed manually at different scalp locations to assess CVR at the respective cerebral vascular territory. We aim to develop soft-computing approaches, e.g. a neuro-fuzzy inference system (Lin and Lee 1996), that will establish consistent clinico-anatomic correlations of CVR (and NVC) of each cerebral vascular territories (Tatu et al. 2012) from NIRS-EEG/HD-tDCS assessments with those corresponding to ASL/TCD assessments

- a scientific contribution enhancing our understanding of interactions between hemodynamic and neuronal responses in health and disease.

## ACKNOWLEDGMENTS

Research conducted within the context of the Franco-German PHC-PROCOPE 2014 funding and Franco-India INRIA-DST funding where the help received from the Indian collaborators (Dr. med. Abhijit Das and Dr. Shubhajit Roy Chowdhury) and students is gratefully acknowledged. Also, the help received from the Neuro Rehab Services LLP and Institute of Neurosciences Kolkata, India in conducting the clinical study is gratefully acknowledged. This project was further supported by the German Ministry for Education and Research (BMBF, Project EYE-TSS 03IPT605E).

## REFERENCES

[1] Dutta A, Nitsche MA. A neural mass model for simulating modulation of cortical activity with transcranial direct current stimulation. In proceeding of: 2013 6th International IEEE/EMBS Conference on Neural Engineering (NER).

[2] Dutta A, Muthalib M, Roy Chowdhury S, Guiraud D, Nitsche MA, Perrey S. Development of an EEG-fNIRS based online monitoring tool towards delivery of non-invasive brain stimulation. In proceeding of: 36th Annual International Conference of the IEEE Engineering in Medicine and Biology Society (EMBC'14), 2014a;.

[3] Dutta A, Roy Chowdhury S, Das A. A Novel Method For Capturing Cerebrovascular Reactivity Using Near-infrared Spectroscopy During Transcranial Direct Current Stimulation: A Stroke Case Series, *30th International Congress of Clinical Neurophysiology* 2014.

[4] Attwell D, Buchan AM, Charpak S, Lauritzen M, Macvicar BA, Newman EA. Glial and neuronal control of brain blood flow. Nature. 2010 Nov 11;468(7321):232–43.

[5] Barbour RL, Graber HL, Xu Y, Pei Y, Schmitz CH, Pfeil DS, et al. A programmable laboratory testbed in support of evaluation of functional brain activation and connectivity. IEEE Trans Neural Syst Rehabil Eng Publ IEEE Eng Med Biol Soc. 2012 Mar;20(2):170–83.

[6] Behzadi Y, Liu TT. An arteriolar compliance model of the cerebral blood flow response to neural stimulus. NeuroImage. 2005 May 1;25(4):1100–11.

[7] Boas DA, Strangman G, Culver JP, Hoge RD, Jasdzewski G, Poldrack RA, et al. Can the cerebral metabolic rate of oxygen be estimated with near-infrared spectroscopy? Phys Med Biol. 2003 Aug 7;48(15):2405–18.

[8] Bos D, Portegies MLP, van der Lugt A, Bos MJ, Koudstaal PJ, Hofman A, et al. Intracranial carotid artery atherosclerosis and the risk of stroke in whites: the Rotterdam Study. JAMA Neurol. 2014 Apr;71(4):405–11.

[9] Bozzo L, Puyal J, Chatton J-Y. Lactate Modulates the Activity of Primary Cortical Neurons through a Receptor-Mediated Pathway. PLoS ONE. 2013 Aug 12;8(8):e71721.

[10] Buxton RB, Frank LR. A model for the coupling between cerebral blood flow and oxygen metabolism during neural stimulation. J Cereb Blood Flow Metab Off J Int Soc Cereb Blood Flow Metab. 1997 Jan;17(1):64–72.

[11] Buzsáki G, Anastassiou CA, Koch C. The origin of extracellular fields and currents--EEG, ECoG, LFP and spikes. Nat Rev Neurosci. 2012 Jun;13(6):407–20.

[12] Carvalhaes CG, Suppes P. A spline framework for estimating the EEG surface laplacian using the Euclidean metric. Neural Comput. 2011 Nov;23(11):2974–3000.

[13] Chander BS, Chakravarthy VS. A Computational Model of Neuro-Glio-Vascular Loop Interactions. PLoS One. 2012 Nov 20;7(11):e48802.

[14] Choi J, Wolf M, Toronov V, Wolf U, Polzonetti C, Hueber D, et al. Noninvasive determination of the optical properties of adult brain: near-infrared spectroscopy approach. J Biomed Opt. 2004 Feb;9(1):221–9.

[15] David O, Friston KJ. A neural mass model for MEG/EEG: coupling and neuronal dynamics. NeuroImage. 2003 Nov;20(3):1743–55.

[16] DeFazio RA, Keros S, Quick MW, Hablitz JJ. Potassium-coupled chloride cotransport controls intracellular chloride in rat neocortical pyramidal neurons. J Neurosci Off J Soc Neurosci. 2000 Nov 1;20(21):8069–76.

[17] Delorme A, Makeig S. EEGLAB: an open source toolbox for analysis of single-trial EEG dynamics including independent component analysis. J Neurosci Methods. 2004 Mar 15;134(1):9–21.

[18] Dhamala M, Rangarajan G, Ding M. Analyzing information flow in brain networks with nonparametric Granger causality. NeuroImage. 2008 Jun;41(2):354–62.

[19] Dmochowski JP, Datta A, Bikson M, Su Y, Parra LC. Optimized multi-electrode stimulation increases focality and intensity at target. J Neural Eng. 2011 Aug;8(4):046011.

[20] Dutta A. EEG-NIRS based low-cost screening and monitoring of cerebral microvessels functionality, *International Stroke Conference 2014*, San Diego, 2014.

[21] Dutta A, Chowdhury SR, Dutta A, Sylaja PN, Guiraud D, Nitsche M. A phenomological model for capturing cerebrovascular reactivity to anodal transcranial direct current stimulation. 2013 6th Int IEEEEMBS Conf Neural Eng NER. 2013. p. 827–30.

[22] Dutta A, Nitsche M. Neural mass model analysis of online modulation of electroencephalogram with transcranial direct current stimulation. 2013 6th Int IEEEEMBS Conf Neural Eng NER. 2013. p. 206–10.

[23] Eckman DM, Nelson MT. Potassium Ions as Vasodilators: Role of Inward Rectifier Potassium Channels. Circ Res. 2001 Feb 2;88(2):132–3.

[24] Edwards D, Cortes M, Datta A, Minhas P, Wassermann EM, Bikson M. Physiological and modeling evidence for focal transcranial electrical brain stimulation in humans: a basis for high-definition tDCS. NeuroImage. 2013 Jul 1;74:266–75.

[25] Filosa JA. Vascular tone and neurovascular coupling: considerations toward an improved in vitro model. Front Neuroenergetics. 2010;2.

[26] Foreman B, Claassen J. Quantitative EEG for the detection of brain ischemia. Crit Care. 2012 Mar 20;16(2):216.

[27] Fricke K, Seeber AA, Thirugnanasambandam N, Paulus W, Nitsche MA, Rothwell JC. Time course of the induction of homeostatic plasticity generated by repeated transcranial direct current stimulation of the human motor cortex. J Neurophysiol. 2011 Mar;105(3):1141–9.

[28] Friston KJ, Mechelli A, Turner R, Price CJ. Nonlinear responses in fMRI: the Balloon model, Volterra kernels, and other hemodynamics. NeuroImage. 2000 Oct;12(4):466–77.

[29] Gagnon L, Cooper RJ, Yücel MA, Perdue KL, Greve DN, Boas DA. Short separation channel location impacts the performance of short channel regression in NIRS. NeuroImage. 2012 Feb 1;59(3):2518–28.

[30] Girouard H, Iadecola C. Neurovascular coupling in the normal brain and in hypertension, stroke, and Alzheimer disease. J Appl Physiol Bethesda Md 1985. 2006 Jan;100(1):328–35.

[31] Gruetter R, Novotny EJ, Boulware SD, Rothman DL, Shulman RG. 1H NMR Studies of Glucose Transport in the Human Brain. J Cereb Blood Flow Metab. 1996 May;16(3):427–38.

[32] Halnes G, Ostby I, Pettersen KH, Omholt SW, Einevoll GT. Electrodiffusive Model for Astrocytic and Neuronal Ion Concentration Dynamics. PLoS Comput Biol [Internet]. 2013 Dec [cited 2014 May 11];9(12).

[33] Heekeren HR, Kohl M, Obrig H, Wenzel R, von Pannwitz W, Matcher SJ, et al. Noninvasive Assessment of Changes in Cytochrome-c Oxidase Oxidation in Human Subjects During Visual Stimulation. J Cereb Blood Flow Metab. 1999 Jun;19(6):592–603.

[34] Holthoff K, Witte OW. Directed spatial potassium redistribution in rat neocortex. Glia. 2000 Feb 1;29(3):288–92.

[35] Huang NE, Shen Z, Long SR, Wu MC, Shih HH, Zheng Q, et al. The empirical mode decomposition and the Hilbert spectrum for nonlinear and non-stationary time series analysis. Proc R Soc Lond Ser Math Phys Eng Sci. 1998 Mar 8;454(1971):903–95.

[36] Hübel N, Schöll E, Dahlem MA. Bistable dynamics underlying excitability of ion homeostasis in neuron models. PLoS Comput Biol. 2014 May;10(5):e1003551.

[37] Huppert TJ, Diamond SG, Franceschini MA, Boas DA. HomER: a review of time-series analysis methods for near-infrared spectroscopy of the brain. Appl Opt. 2009 Apr 1;48(10):D280–298.

[38] Iadecola C. Neurovascular regulation in the normal brain and in Alzheimer's disease. Nat Rev Neurosci. 2004 May;5(5):347–60.

[39] Islam N, Aftabuddin M, Moriwaki A, Hattori Y, Hori Y. Increase in the calcium level following anodal polarization in the rat brain. Brain Res. 1995 Jul 3;684(2):206–8.

[40] Jann K, Koenig T, Dierks T, Boesch C, Federspiel A. Association of individual resting state EEG alpha frequency and cerebral blood flow. NeuroImage. 2010 May 15;51(1):365–72.

[41] Kuo H-I, Bikson M, Datta A, Minhas P, Paulus W, Kuo M-F, et al. Comparing cortical plasticity induced by conventional and high-definition 4 × 1 ring tDCS: a neurophysiological study. Brain Stimulat. 2013 Jul;6(4):644–8.

[42] Lang N, Siebner HR, Ernst D, Nitsche MA, Paulus W, Lemon RN, et al. Preconditioning with transcranial direct current stimulation sensitizes the motor cortex to rapid-rate transcranial magnetic stimulation and controls the direction of after-effects. Biol Psychiatry. 2004 Nov 1;56(9):634–9.

[43] Lanzino G, Rabinstein AA, Brown RD. Treatment of Carotid Artery Stenosis: Medical Therapy, Surgery, or Stenting? Mayo Clin Proc. 2009 Apr;84(4):362–8.

[44] Lareau E, Simard G, Lesage F, Nguyen D, Sawan M. Near infrared spectrometer combined with multichannel EEG for functional brain imaging. 2011 5th Int Symp Med Inf Commun Technol ISMICT. 2011. p. 122–6.

[45] LeMasson G, Marder E, Abbott LF. Activity-dependent regulation of conductances in model neurons. Science. 1993 Mar 26;259(5103):1915–7.

[46] Leontiev O, Buxton RB. Reproducibility of BOLD, perfusion, and CMRO2 measurements with calibrated-BOLD fMRI. NeuroImage. 2007 Mar;35(1):175–84.

[47] Lin C-T, Lee CSG. Neural Fuzzy Systems: A Neuro-Fuzzy Synergism to Intelligent Systems. Har/Dsk edition. Upper Saddle River, NJ: Prentice Hall; 1996.

[48] Lin WH, Hao Q, Rosengarten B, Leung WH, Wong KS. Impaired neurovascular coupling in ischaemic stroke patients with large or small vessel disease. Eur J Neurol Off J Eur Fed Neurol Soc. 2011 May;18(5):731–6.

[49] Ljung L. System Identification: Theory for the User. 2 edition. Upper Saddle River, NJ: Prentice Hall; 1999.

[50] Lucas SJE, Tzeng YC, Galvin SD, Thomas KN, Ogoh S, Ainslie PN. Influence of Changes in Blood Pressure on Cerebral Perfusion and Oxygenation. Hypertension. 2010 Mar 1;55(3):698–705.

[51] Lüscher C, Malenka RC. NMDA receptor-dependent long-term potentiation and long-term depression (LTP/LTD). Cold Spring Harb Perspect Biol. 2012 Jun;4(6).

[52] Malenka RC, Bear MF. LTP and LTD: an embarrassment of riches. Neuron. 2004 Sep 30;44(1):5–21.

[53] Markus H, Cullinane M. Severely impaired cerebrovascular reactivity predicts stroke and TIA risk in patients with carotid artery stenosis and occlusion. Brain. 2001 Mar 1;124(3):457–67.

[54] Meeks JP, Mennerick S. Selective effects of potassium elevations on glutamate signaling and action potential conduction in hippocampus. J Neurosci Off J Soc Neurosci. 2004 Jan 7;24(1):197–206.

[55] Sood M, Jindal U, Das A, Dutta A, Roy Chowdhury S. Continuous wave functional near infra-red spectroscopy combined with transcranial direct current stimulation for assessment of cerebral vascular status in patients with ischemic stroke. In proceeding of: fNIRS2014, At Montreal, Canada 2014;

[56] Mikulis DJ. Chronic Neurovascular Uncoupling Syndrome. Stroke. 2013 Jun 1;44(6 suppl 1):S55–7.

[57] Miranda PC, Mekonnen A, Salvador R, Ruffini G. The electric field in the cortex during transcranial current stimulation. NeuroImage. 2013 Apr 15;70:48–58.

[58] Molaee-Ardekani B, Márquez-Ruiz J, Merlet I, Leal-Campanario R, Gruart A, Sánchez-Campusano R, et al. Effects of transcranial Direct Current Stimulation (tDCS) on cortical activity: A computational modeling study. Brain Stimulat. 2013 Jan;6(1):25–39.

[59] Moran RJ, Kiebel SJ, Stephan KE, Reilly RB, Daunizeau J, Friston KJ. A neural mass model of spectral responses in electrophysiology. NeuroImage. 2007 Sep 1;37(3):706–20.

[60] Müller JFM, Orekhov Y, Liu Y, Ziemann U. Homeostatic plasticity in human motor cortex demonstrated by two consecutive sessions of paired associative stimulation. Eur J Neurosci. 2007 Jun;25(11):3461–8.

[61] Nikulin VV, Fedele T, Mehnert J, Lipp A, Noack C, Steinbrink J, et al. Monochromatic Ultra-Slow (~0.1Hz) Oscillations in the human electroencephalogram and their relation to hemodynamics. NeuroImage. 2014 Apr 13;

[62] Nitsche MA, Fricke K, Henschke U, Schlitterlau A, Liebetanz D, Lang N, et al. Pharmacological modulation of cortical excitability shifts induced by transcranial direct current stimulation in humans. J Physiol. 2003 Nov 15;553(Pt 1):293–301.

[63] Nitsche MA, Paulus W. Excitability changes induced in the human motor cortex by weak transcranial direct current stimulation. J Physiol. 2000 Sep 15;527 Pt 3:633–9.

[64] Nunez PL, Srinivasan R. Electric Fields of the Brain: The Neurophysics of EEG. Oxford University Press; 2006. 629 p.

[65] Paraskevas KI, Spence JD, Veith FJ, Nicolaides AN. Identifying Which Patients With Asymptomatic Carotid Stenosis Could Benefit From Intervention. Stroke J Cereb Circ. 2014 Oct 30;

[66] Pellerin L, Magistretti PJ. Glutamate uptake into astrocytes stimulates aerobic glycolysis: a mechanism coupling neuronal activity to glucose utilization. Proc Natl Acad Sci U S A. 1994 Oct 25;91(22):10625–9.

[67] Perrin F, Pernier J, Bertrand O, Echallier JF. Spherical splines for scalp potential and current density mapping. Electroencephalogr Clin Neurophysiol. 1989 Feb;72(2):184–7.

[68] Radman T, Ramos RL, Brumberg JC, Bikson M. Role of cortical cell type and morphology in subthreshold and suprathreshold uniform electric field stimulation in vitro. Brain Stimulat. 2009 Oct;2(4):215–228, 228.e1–3.

[69] Rahman A, Reato D, Arlotti M, Gasca F, Datta A, Parra LC, et al. Cellular effects of acute direct current stimulation: somatic and synaptic terminal effects. J Physiol. 2013 May 15;591(Pt 10):2563–78.

[70] Safaie J, Grebe R, Abrishami Moghaddam H, Wallois F. Toward a fully integrated wireless wearable EEG-NIRS bimodal acquisition system. J Neural Eng. 2013 Oct;10(5):056001.

[71] Scholkmann F, Kleiser S, Metz AJ, Zimmermann R, Mata Pavia J, Wolf U, et al. A review on continuous wave functional near-infrared spectroscopy and imaging instrumentation and methodology. NeuroImage. 2014 Jan 15;85 Pt 1:6–27.

[72] Sheorajpanday RVA, Nagels G, Weeren AJTM, van Putten MJAM, De Deyn PP. Reproducibility and clinical relevance of quantitative EEG parameters in cerebral ischemia: a basic approach. Clin Neurophysiol Off J Int Fed Clin Neurophysiol. 2009 May;120(5):845–55.

[73] Siebner HR, Lang N, Rizzo V, Nitsche MA, Paulus W, Lemon RN, et al. Preconditioning of low-frequency repetitive transcranial magnetic stimulation with transcranial direct current stimulation: evidence for homeostatic plasticity in the human motor cortex. J Neurosci Off J Soc Neurosci. 2004 Mar 31;24(13):3379–85.

[74] Siesler HW, Ozaki Y, Kawata S, Heise HM. Near-Infrared Spectroscopy: Principles, Instruments, Applications. John Wiley & Sons; 2008. 365 p.

[75] Soraghan C, Matthews F, Markham C, Pearlmutter BA, O'Neill R, Ward TE. A 12-channel, real-time near-infrared spectroscopy instrument for brain-computer interface applications. Conf Proc Annu Int Conf IEEE Eng Med Biol Soc IEEE Eng Med Biol Soc Annu Conf. 2008;2008:5648–51.

[76] Sotero RC, Trujillo-Barreto NJ, Iturria-Medina Y, Carbonell F, Jimenez JC. Realistically coupled neural mass models can generate EEG rhythms. Neural Comput. 2007 Feb;19(2):478–512.

[77] Stagg CJ, Nitsche MA. Physiological basis of transcranial direct current stimulation. Neurosci Rev J Bringing Neurobiol Neurol Psychiatry. 2011 Feb;17(1):37–53.

[78] Stoll M, Hamann GF. [Cerebrovascular reserve capacity]. Nervenarzt. 2002 Aug;73(8):711–8.

[79] Tatu L, Moulin T, Vuillier F, Bogousslavsky J. Arterial territories of the human brain. Front Neurol Neurosci. 2012;30:99–110.

[80] Turrigiano GG. The self-tuning neuron: synaptic scaling of excitatory synapses. Cell. 2008 Oct 31;135(3):422–35.

[81] Ursino M, Cona F, Zavaglia M. The generation of rhythms within a cortical region: analysis of a neural mass model. NeuroImage. 2010 Sep;52(3):1080–94.

[82] Verkhratsky A, Orkand RK, Kettenmann H. Glial Calcium: Homeostasis and Signaling Function. Physiol Rev. 1998 Jan 1;78(1):99–141.

[83] Vernieri F, Assenza G, Maggio P, Tibuzzi F, Zappasodi F, Altamura C, et al. Cortical neuromodulation modifies cerebral vasomotor reactivity. Stroke J Cereb Circ. 2010 Sep;41(9):2087–90.

[84] Villringer A, Chance B. Non-invasive optical spectroscopy and imaging of human brain function. Trends Neurosci. 1997 Oct;20(10):435–42.

[85] Viswanathan A, Freeman RD. Neurometabolic coupling in cerebral cortex reflects synaptic more than spiking activity. Nat Neurosci. 2007 Oct;10(10):1308–12.

[86] Williams A, O'Leary T, Marder E. Homeostatic Regulation of Neuronal Excitability. Scholarpedia. 2013;8(1):1656.

[87] Yang J, Ruchti E, Petit J-M, Jourdain P, Grenningloh G, Allaman I, et al. Lactate promotes plasticity gene expression by potentiating NMDA signaling in neurons. Proc Natl Acad Sci. 2014 Aug 19;111(33):12228–33.

[88] Zavaglia M, Astolfi L, Babiloni F, Ursino M. A neural mass model for the simulation of cortical activity estimated from high resolution EEG during cognitive or motor tasks. J Neurosci Methods. 2006 Oct 30;157(2):317–29.

[89] Zheng X, Alsop DC, Schlaug G. Effects of transcranial direct current stimulation (tDCS) on human regional cerebral blood flow. NeuroImage. 2011 Sep 1;58(1):26–33.

[90] Zhou D, Thompson WK, Siegle G. MATLAB toolbox for functional connectivity. NeuroImage. 2009 Oct 1;47(4):1590–607.